Michael Jaeger, Kujtim Gashi, Hidayet Günhan Akarçay, Gerrit Held, Sara Peeters,
Tigran Petrosyan, Stefan Preisser, Michael Gruenig and Martin Frenz*

Real-time clinical clutter reduction in combined epi-optoacoustic and ultrasound imaging

Echtzeit-Clutter-Reduktion bei kombinierter epi-optoakustischer und Ultraschall-Bildgebung

Abstract: Flexible imaging of the human body, a requirement for broad clinical application, is obtained by direct integration of optoacoustic (OA) imaging with echo ultrasound (US) in a multimodal epi-illumination system. Up to date, successful deep epi-OA imaging is difficult to achieve owing to clutter. Clutter signals arise from optical absorption in the region of tissue irradiation and strongly reduce contrast and imaging depth. Recently, we developed a displacement-compensated averaging (DCA) technique for clutter reduction based on the clutter decorrelation that occurs when palpating the tissue. To gain first clinical experience on the practical value of DCA, we implemented this technique in a combined clinical OA and US imaging system. Our experience with freehand scanning of human volunteers reveals that real-time feedback on the clutter-reduction outcome is a key factor for achieving superior contrast and imaging depth.

Keywords: photoacoustics; diagnostic imaging; contrast; imaging depth.

Zusammenfassung: Die direkte Integration der optoakustischen Beleuchtung in einen Ultraschallkopf zu einem multimodalen bildgebenden Diagnosegerät erlaubt eine flexible Bildgebung des menschlichen Körpers. Diese Flexibilität stellt eine wichtige Voraussetzung für eine breite klinische Anwendung dar. Infolge von Clutter ist es bis heute jedoch schwierig, optoakustische Bilder aus großer Tiefe im Gewebe zu gewinnen. Clutter, der durch optische Absorption im Bereich der Lichteinstrahlung im Gewebe entsteht, führt zu einer starken Verringerung des Kontrastes und zu einer deutlichen Reduktion der Bildtiefe. In den letzten Jahren entwickelten wir eine Methode, das sogenannte „displacement compensated averaging" (DCA), um diesen Clutter zu reduzieren. Dabei wird das Gewebe mechanisch leicht verschoben, was bei der Mittelung der einzelnen Bilder zu einer Dekorrelation des Clutters führt. Um erste praktische Erfahrungen mit DCA zu gewinnen, integrierten wir dieses Verfahren in ein klinisches optoakustisches und Ultraschall-Gerät. Unsere Messungen im Freihand-Scan-Modus an Probanden zeigte, dass eine Clutterreduktion in Echtzeit einen Schlüsselfaktor für die Verbesserung des Kontrastes und der Bildtiefe darstellt.

Schlüsselwörter: Photoakustik; diagnostische Bildgebung; Kontrast; Bildtiefe.

*Corresponding author: Martin Frenz, Institute of Applied Physics, University of Bern, Sidlerstrasse 5, 3012 Bern, Switzerland, e-mail: frenz@iap.unibe.ch
Michael Jaeger, Hidayet Günhan Akarçay, Gerrit Held, Sara Peeters, Tigran Petrosyan, Stefan Preisser and Michael Gruenig: Institute of Applied Physics, University of Bern, Sidlerstrasse 5, 3012 Bern, Switzerland
Kujtim Gashi: Institute of Applied Physics, University of Bern, Sidlerstrasse 5, 3012 Bern, Switzerland; and Technische Universiteit Eindhoven, Den Dolech 2, 5612 AZ Eindhoven, The Netherlands

1 Introduction

Optoacoustic (OA) imaging allows visualizing absorbing structures inside optically turbid tissue based on detection of thermoelastic pressure waves after short-pulsed laser irradiation [1–10]. In a multi-modal combination with pulse-echo ultrasound (US) [11–19], OA imaging is promising to improve diagnostic accuracy [20–22] via the display of small blood vessels [12] or the local blood oxygenation level [23]. Clinically, an adequate imaging depth of several centimeters is required to monitor and diagnose breast cancer, cardiovascular disease, or vascular recovery after severe trauma or burns. Such an imaging depth can theoretically be achieved when only transducer noise and optical penetration depth must be considered

[24] as experimentally demonstrated in volunteer studies when using transmission [25, 26] or orthogonal mode [20] OA tomography. Tomographic set-ups, however, lack the flexibility of freehand scanning, require dedicated stand-alone equipment, and can only be employed for acoustically transparent tissues such as the breast. On the contrary, multimodal combined OA and US imaging is preferably performed in an epi-style set-up with the irradiation optics and acoustic transducer integrated into one single-combined probe. In that way it can flexibly access any part of the human body that is already available to conventional US with freehand probe guidance. Unfortunately, a suitable clinical imaging depth has up to date been hard to achieve with epi-OA imaging. The main reason is that epi-OA imaging contrast is limited in addition to thermal noise by significant clutter [15, 27–29]. This clutter is thought to arise from strong OA transients that are generated at the site of tissue irradiation, and are detected (*i*) after direct propagation to the imaging probe (direct clutter), or (*ii*) after being scattered by acoustic inhomogeneities located within the imaging plane (echo clutter).

As a possible solution to improve epi-OA imaging depth towards noise-limited imaging, we have previously proposed deformation (or displacement)-compensated averaging (DCA) for clutter reduction [28]. In DCA, dynamical deformation of the investigated tissue when palpating the skin surface with probe motion parallel to the imaging plane leads to clutter decorrelation. When compensating the OA image for the geometrical distortion caused by the deformation, sequential averaging of consecutive images conserves true OA features but the decorrelating clutter is reduced like stochastic noise. In combined OA and US imaging, motion tracking of US images provides the knowledge of local tissue displacement that is required for OA deformation compensation. *In-vitro* tissue [28] and gelatin phantom [29] studies, having realistic echogenicity in addition to the optical properties, have consistently shown that DCA significantly improves imaging depth in comparison to conventional averaging without probe motion. These experiments were performed with controlled probe motion using motorized stages. In addition, first free-hand experiments with human volunteers have confirmed that clutter is significant in clinical epi-OA images and that DCA can help to improve image contrast [15]. However, this set-up was limited in its clinical applicability because the used equipment did not allow real-time display of DCA-processed OA images and thus no feedback on the clutter reduction performance was available. In addition, optoacoustically generated pulse-echo images had to be used for motion tracking,

limiting the tracking accuracy and thus the clutter reduction performance.

The aim of the present study was to gain experience with a clinical system which offers state-of-the-art US motion tracking and real-time display of the DCA processing result allowing physicians to optimize the probe motion. For this purpose we have implemented real-time DCA in combined epi-OA and US imaging on a research US system. Our results of real-time OA clutter reduction in freehand scanning of human volunteers confirm the importance of clutter reduction, and our experience reveals that real-time display is essential for achieving optimum results.

2 Materials and methods

We implemented combined real-time OA and US imaging using a Verasonics® (VS) system (Verasonics Inc., Redmond, WA, USA). This research system offered simultaneous US transmission on 128 elements (two-board version) and signal acquisition from 64 elements of an array probe. Fast data transfer from the data acquisition system via a PCI Express link to a 12 core host PC allowed continuous subsequent data processing (image reconstruction, DCA, and display). We implemented a dedicated MatLab script for the acquisition of both US and OA data from a HDI L7-4 broadband linear vascular probe (ATL Philips, Bothell, WA, USA). This probe features 128 elements at 0.29 mm pitch, and a bandwidth from 4 to 7 MHz with 5 MHz center frequency. A sampling rate of 20 MHz was chosen for signal acquisition. For OA imaging, we used a Q-switched Nd:YAG laser (Brilliant B; Quantel, France) at 1064 nm wavelength, tuned to provide laser pulses with 5 ns pulse length and 120 mJ pulse energy at 10 Hz pulse repetition rate. A custom-made bifurcated fiber bundle (Fiberoptic P. & P. AG, Spreitenbach, Switzerland) terminating into two line profile converters was applied to transmit the laser light. The profile converters were fixated to either side of the acoustic probe to irradiate the tissue through two line profiles with 20 mm length (parallel to the linear array) and 5 mm width, resulting in a total irradiation area of 2 cm^2 with a maximum radiant exposure of 60 mJ/cm^2. For a detailed theoretical background of DCA we refer to [28]. Briefly, DCA comprises motion tracking of US images, which are acquired alternately to OA images for the determination of the two-dimensional (2D) distribution of the local displacement of the tissue relative to the probe aperture. The displacement information is used for deformation compensation of the OA images prior to averaging. For the implementation of real-time DCA, the acquisition

sequence and the processing chain were designed as follows: The sequence started with the acquisition of an OA data frame (US transmit switched off), triggered by the flashlamp of the laser system. An internal delay was set in the VS script to synchronize the signal acquisition start with the laser pulse generation. Parallel acquisition on the middle 64 elements of the array probe provided an effective aperture of 18.9 mm. After a delay of 100 μs, sufficient for both OA signal acquisition and data transfer to the PC, the VS triggered the acquisition of a US data frame. This acquisition included a sequence of 32 transmit and receive events to scan a region of 18.9 mm (laterally) by 30 mm (axially) with a focused US beam (focal length 30 mm) in a classical line-by-line approach. The data were stored in the local memory and transferred to the PC after the acquisition was completed. The total duration for the US acquisition was 6.4 ms, which is insignificant compared to the 100 ms time interval between two consecutive OA acquisitions. After data transfer a line-by-line US image was obtained using Verasonics' proprietary pixel-based algorithm. Then, OA image reconstruction was performed, using our frequency-domain algorithm [30] coded in MatLab. The subsequent DCA processing (US-based displacement tracking, motion compensation and averaging of OA images) was also programmed in MatLab. It is of note, that data processing was performed on a PC, and was running in parallel to the data acquisition that was controlled by the VS system. The described sequence (acquisition, processing) was repeated with each laser pulse, and the results were continuously displayed on the screen while performing the *in vivo* experiments.

The aim of this study was to provide early experience with real-time DCA in a clinically realistic scanning scenario, therefore MatLab was chosen for convenient and straight-forward implementation of DCA. To keep the system real-time, several simplifications were made to the processing chain to reduce computational complexity. The foundation of all the simplifications described in the following is the fact that, when using a clinical system, the signal bandwidth in both US and OA imaging is limited by the comparably narrow transducer bandwidth (60% of center frequency, whereas a broadband transducer would have 200% bandwidth). The narrowband signal can be factored into a sinusoidal carrier at the transducers center frequency and a slowly varying envelope. The first simplification was thus made to OA image reconstruction. Conventionally, OA images would be reconstructed from the real-valued radio-frequency (RF) signal data that was acquired, in our case, at 20 MHz sampling rate. In order to reduce the numerical burden, we performed image reconstruction on the analytic (complex) signal, derived via

the Hilbert transform from the RF signal. In the analytic signal, the arrival time and amplitude of OA transients are accurately coded in the complex phase and the amplitude of the envelope, respectively. Both vary on a slower temporal scale than the carrier does, allowing down sampling to a rate of 5 MHz prior to OA image reconstruction. This procedure resulted in a strongly improved reconstruction speed without significant loss of image quality. Various techniques are available for US-based motion tracking of both axial as well as lateral motion, enabling motion compensation for compressive as well as shear deformation. However, for the sake of computational efficiency, a second simplification was made to the data processing chain by employing base-band correlation [31] for motion tracking. In this approach, it is assumed that tissue motion occurs only in axial direction. The base-band representations $u_1(x, z)$ and $u_2(x, z)$ [result of the in-phase quadrature (IQ) conversion, i.e., Hilbert transform and demodulation] of two successive reconstructed pulse-echo frames are:

$$u_1(x,z) = A(x,z)$$
$$u_2(x,z) = A(x, z\text{-}\Delta z(x,z)) \cdot e^{-2\pi i \frac{\Delta z(x,z)}{0.5\lambda}} \tag{1}$$

where x and z are the lateral and the axial coordinates, respectively, of the imaging plane; $A(x, z)$ is the complex envelope (base-band) of the first frame; λ is the acoustic wavelength at the center frequency of the linear probe (carrier frequency); and Δz is the local tissue displacement in axial direction in-between the two acquisitions. Because the spatial variation of the complex envelope is slow compared to the oscillation of the carrier, and for displacements smaller than a quarter acoustic wavelength, the phase of the point-wise Hermitian product of the base-band frames translates directly into the local displacement:

$$u_1(x,z) \cdot u_2^*(x,z) = A(x,z) \cdot A^*(x, z\text{-}\Delta z(x,z)) \cdot e^{2\pi i \frac{\Delta z(x,z)}{0.5\lambda}}$$
$$\cong |A(x,z)|^2 \cdot e^{2\pi i \frac{\Delta z(x,z)}{0.5\lambda}}$$
$$\Rightarrow \arg[u_1(x,z) \cdot u_2^*(x,z)] \cdot \frac{0.5\lambda}{2\pi i} \cong \Delta z(x,z). \tag{2}$$

For its computational simplicity, this technique offers real-time tracking of the local axial displacement using MatLab. To achieve robust tracking, the argument was taken after low-pass filtering of the Hermitian product by convolution with a rectangular tracking kernel (size: 3×3 mm). This method allowed accurate tracking of the local axial displacement with high accuracy as long as the displacements were smaller than a quarter (~75 μm) of the acoustic wavelength (~300 μm) at the center frequency (5

MHz) to avoid phase wrapping. To be able to track even larger displacements with similar efficiency, we further developed the technique to a multi-scale approach. For this purpose, the squared absolute envelope of the reconstructed frame was band-pass filtered in axial direction, to synthesize RF data having a center frequency (2.5 MHz) lower than the probe's center frequency. These data were processed in the same way as the original data [IQ conversion, displacement tracking according to Eqn. (2)], for obtaining a rough estimate of the axial displacements up to 150 μm. In a second step, the original data were used for fine tracking, without the ambiguity linked to phase wrapping. At 10 Hz frame rate, 150 μm maximum displacement in-between successive frames corresponded to a maximum motion velocity of 1.5 mm/s, a limitation which could easily be fulfilled when scanning the forearm with freehand probe motion. Subsequent displacements were accumulated to obtain the total local axial displacement relative to a starting reference frame. Because no lateral tracking was possible with this technique, only axial probe motion (compression and dilation) could be employed for DCA.

A third reduction of numerical complexity was achieved by performing deformation compensation on the base-band representation of the reconstructed OA frames (result of IQ conversion). Such a baseband presentation is again possible because the signal bandwidth is determined by the transducer rather than by the frequency content of the OA transients, and it is the direct result of the reconstruction described above. With $p_1(x, z)$ being the base-band representation of a starting OA frame, successive OA frames can be modeled as:

$$p_1(x,z) = P(x,z) + C(x,z,1)$$
$$p_k(x,z) = P(x,z - \Delta z(x,z,k)) \cdot e^{-2\pi i \frac{\Delta z(x,z,k)}{\lambda}} + C(x,z,k). \quad (3)$$

$P(x, z)$ is the base-band representation of the first acquisition without clutter, p_k is the base-band representation of the k-th acquisition including the respective clutter realization $C(x, z, k)$, and $\Delta z(x, z, k)$ is the local displacement at the time of the k-th acquisition relative to the first acquisition. The compensated frames $p_{k,comp}$ were obtained according to:

$$p_{k,comp}(x,z) = p_k(x,z + \Delta z(x,z,k)) \cdot e^{2\pi i \frac{\Delta z(x,z,k)}{\lambda}}$$
$$= P(x,z) + C(x,z + \Delta z(x,z,k),k) \cdot e^{2\pi i \frac{\Delta z(x,z,k)}{\lambda}}. \quad (4)$$

A moving time average of successive deformation-compensated OA base-band frames was then calculated to yield the DCA-OA frame. This averaging led to reduction

of the clutter component, by decorrelation of $C(..., k)$, but also by phase cancellation of the oscillating complex exponential. An exponential moving average was chosen with averaging weights corresponding to an averaging time constant of 2 s (20 frames). The same deformation compensation was applied to the US frames prior to display, to obtain US frames that were co-registered with the DCA-OA frames. US frames and DCA-OA frames were continuously displayed, after envelope detection (absolute value of the base-band representation) and logarithmic compression of the envelope. A compression range of 60 dB and 40 dB was chosen for the US image and the OA image, respectively. In addition the displacement map was displayed for control. With the described simplifications, the speed of the PC was sufficient for image reconstruction, DCA processing and continuous display of OA and US images at a rate of 10 Hz equal to the laser pulse rate.

Using this system, we evaluated real-time DCA clutter reduction in freehand scanning of human volunteers. For a trustworthy comparison of DCA to conventional averaging, each imaging location was in a first step imaged without displacement until the continuously averaged OA image converged to a stable result (reference image). In a second step, the tissue was slightly compressed and released with repetitive probe motion in axial direction, until best clutter reduction was achieved under real-time feedback (DCA image).

3 Results

Figure 1 exemplary shows results that were obtained at different locations on a volunteers forearm. B-mode US images are presented in the first column as a reference to provide an impression of the anatomical context. The subcutaneous fat layer is seen (marked as "F") as well as muscle epimysia (marked as "E") and the ulnar nerve (marked as "UN") in Figure 1A. The second column shows the reference OA images and the third column the DCA results. All examples consistently reveal a strong contrast improvement when using DCA. The fact that the same number of averages was used for both the reference and DCA demonstrates that this contrast improvement is not an effect of averaging of stochastic noise, but of decorrelation with probe motion of some kind of systematic background. At the same time, all DCA images show distinct details that are also present in the reference images. The fact that the relative intensity level of background signal in comparison to OA detail was reduced by DCA suggests that the background did not correspond to true OA
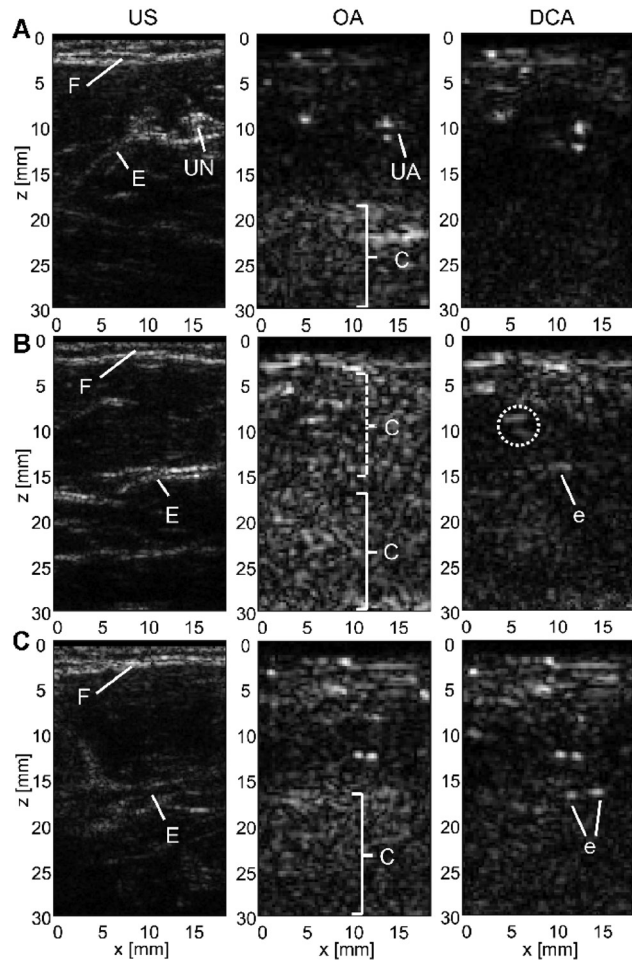
Figure 1 Results of real-time combined ultrasound (US; first column), conventional optoacoustic (OA; second column) and displacement-compensated averaging (DCA; third column) opto-acoustic imaging obtained at three different imaging locations on a volunteers forearm (A–C).

F, subcutaneous fat layer; E, muscle epimysia; UN, ulnar nerve; UA, ulnar artery; e, thin blood vessel; C, clutter.

sources located in the imaging plane. By definition, such background signal is clutter. We hypothesize that a large part of this clutter was caused by the strong OA transients that were generated at the location of tissue irradiation, outside the imaging plane. The main clutter in Figure 1A and C (marked with "C" plus bracket) is found at a depth below 15 mm, which corresponds to the separation distance between the irradiation line profiles and the imaging plane of the US transducer [32, 33]. In contrast, the clutter in the OA image (Figure 1B) seems to be homogeneously distributed over the entire imaging depth. This different appearance can be explained by clutter that emerged from acoustic reverberations of OA transients generated by strong optical absorption (e.g., by a pigmented spot such as a mole) directly below the transducer, rather than

at the site of irradiation. Such clutter appears directly below the skin surface (marked with "C" plus dashed bracket) obscuring sub-surface OA details [33], which directly passes into the echo clutter below 15 mm depth that emerged from the irradiation site (marked with "C" plus solid bracket).

Independent of the source of clutter, our results consistently show that the DCA improved the visibility of OA details. Figure 1A is an example of how DCA helps identifying signal to be clutter (strong signal at 22 mm depth), which could also be misinterpreted as true OA signal. This effect of DCA is beneficial, even in situations where the imaging depth is not apparently increased e.g., because of the absence of true absorbing structures. In addition, contrast around the ulnar artery (marked as "UA") which runs in parallel to the ulnar nerve ("UN") was greatly improved.

Figure 1B is an example where the contrast was strongly improved by DCA around details that were already visible in the reference (e.g., the detail marked by dotted circle). This greatly helps identifying true details as such, and allows finding details that were not visible before in the same depth range. An example is the detail marked as "e", which might be one or more thin blood vessels that run along the epimysium ("E") in the corresponding US image.

Figure 1C finally is a good example where imaging depth was clearly improved. The two bright dot structures visible at 16 mm depth in the DCA image (marked as "e") were fully obscured by clutter in the conventional OA image.

4 Discussion

Our first experience with real-time DCA in combined OA and US imaging is promising. In agreement with previous phantom and volunteer studies, the results confirm that DCA significantly improves OA image depth and contrast, and allows to differentiate between background and real OA signals. The described implementation facilitated clutter reduction in freehand imaging requiring only a basic level of practice, which demonstrates the clinical practicability of this technique. The real-time feedback feature was, however, crucial for a good outcome, since it allowed optimizing the probe motion on the fly without limiting the flexibility of freehand probe guidance. Real-time feedback is an essential requirement for two reasons: Firstly, it enables the physician to minimize out-of-plane motion based on observing the US image. Out-of-plane motion would lead to US motion tracking errors

on one hand, and to decorrelation of true OA details on the other hand. The consequence of both is decorrelation of OA detail in the motion-compensated images, resulting in reduced signal level in the DCA image and thus in inferior final contrast. Secondly, real-time display of the DCA result allows optimization of the motion speed. Low speed results in slow decorrelation of the clutter background and thus in suboptimal clutter reduction. A too large speed, on the other hand, results in a large accumulative tissue deformation over the duration of the averaging time constant, and thus to significant out-of-plane motion and re-arrangement of tissue layers with the aforementioned deterioration of image contrast. Based on experience with the proposed real-time implementation, we were able to develop a palpation technique for maximizing the clutter reduction performance under real-time feedback of the DCA result: The tissue is compressed and released using undulatory probe motions, with a cycle length that approximately matches twice the averaging time constant. The motion amplitude is gradually adapted to achieve the best contrast improvement. Optimum freehand probe guidance calls for some practice from the clinician. The level of difficulty, however, was not different from what is already state-of-the-art in clinical quasi-static US elastography.

The presented DCA system prototype was implemented in MatLab in order to achieve early results in a clinically realistic scenario. Several simplifications had to be made to the processing chain in order to achieve real-time imaging as explained in the "Materials and methods" section. Most significantly, US motion tracking was based on base-band correlation, which can only quantify axial tissue motion. As a consequence only axial probe motion (tissue compression and release) could be employed for DCA clutter reduction. When coded in C++, a more complex algorithm would allow 2-D motion tracking which would in turn enable lateral in addition to axial motion compensation. It is expected that lateral probe motion, and thus shear deformation of the tissue, results in improved DCA performance compared to compressive deformation. One of the reasons is that compressive deformation is more likely to result in out-of-plane motion at slippery interfaces between e.g., muscle epimysia, or between glands and surrounding tissue. The other reason is that echo clutter tends to move at a similar speed as true signals in compression mode, whereas the displacement rate is roughly half the displacement rate of true signals in shear mode [29]. Therefore shear deformation will allow for more efficient

separation between true signal and echo clutter. A full implementation of DCA for clinical purposes should therefore aim at real-time 2-D echo tracking and motion compensation.

In the present study, OA image reconstruction and subsequent motion compensation were performed on the analytic OA signal after Hilbert transform and down sampling. This approach of data reduction was reasonable because the limited bandwidth of the transducer eliminated the slow frequencies that are typically contained in OA transients, and only part of the spectrum contained actual information. When using linear array probes, a lower band limit is required to provide narrow focusing in elevation in order to achieve a well-defined imaging plane. When using 2-D array probes, on the other hand, elevation beam-steering is possible and the acoustic receivers can be designed to also detect the low frequencies. The proposed technique is not applicable to the resulting broadband data. However, we would like to point out that clutter is more significant with the stronger US scattering at the higher US frequencies. When the goal is to selectively reduce clutter in a frequency range of interest, then artificially limiting the signal bandwidth might be a valuable way to increase DCA processing speed. The proposed technique of data reduction could then be employed, or alternatively other ways of data reduction could be considered, such as wavelet decomposition.

5 Conclusion

The presented implementation of DCA demonstrates for the first time the practicability of this clutter reduction technique in a clinically realistic scenario of real-time freehand combined epi-OA and US imaging. Apart from confirming significant OA contrast improvement in DCA processing as compared to conventional averaging, our first experience shows that the real-time feedback feature is crucial for the clinical success of DCA because it allows optimizing the probe motion on the fly without limiting the flexibility of freehand probe guidance.

References

[1] Sigrist MW. Laser generation of acoustic waves in liquids and gases. J Appl Phys 1986;60:R83–121.

[2] Oraevsky AA, Jacques SL, Tittel FK. Determination of tissue optical properties by time-resolved detection of laser-induced stress waves. Proc SPIE 1993;1882:86–101.

[3] Oraevsky AA, Jacques SL, Esenaliev RO, Tittel FK. Laser-based optoacoustic imaging in biological tissues. Proc SPIE 1994;2134A:122–8.

[4] Kruger RA, Liu P. Photoacoustic ultrasound: Theory and experimental results. Proc SPIE 1994;2134A:114–21.

[5] Wang LV, Hu S. Photoacoustic tomography: in vivo imaging from organelles to organs. Science 2012;335(6075):1458–62.

[6] Cox B, Laufer JG, Arridge SR, Beard PC. Quantitative spectroscopic photoacoustic imaging: a review. J Biomed Opt 2012;17(6):061202.

[7] Beard P. Biomedical photoacoustic imaging. Int Focus 2011;1(4):602–31.

[8] Köstli KP, Frenz M, Weber HP, Paltauf G, Schmidt-Kloiber H. Optoacoustic tomography: time-gated measurement of pressure distributions and image reconstruction. Appl Opt 2001;40(22):3800–9.

[9] Xu M, Wang LV. Photoacoustic imaging in biomedicine. Rev Sci Instrum 2006;77:41101. http://labs.seas.wustl.edu/bme/wang/epub/2006mxu-pa-review.pdf [Accessed on July 29, 2014].

[10] Hu S, Wang LV. Photoacoustic imaging and characterization of the microvasculature. J Biomed Opt 2010;15(1):011101.

[11] Niederhauser JJ, Jaeger M, Frenz M. Comparison of laser-induced and classical ultrasound. Proc SPIE 2003;4960:118–23.

[12] Niederhauser JJ, Jaeger M, Lemor R, Weber P, Frenz M. Combined ultrasound and optoacoustic system for real-time high-contrast vascular imaging in vivo. IEEE Trans Med Imaging 2005;24(4):436–40.

[13] Kolkman RG, Brands PJ, Steenbergen W, van Leeuwen TG. Real-time in vivo photoacoustic and ultrasound imaging. J Biomed Opt 2008;13(5):050510.

[14] Aguirre A, Guo P, Gamelin J, Yan S, Sanders MM, Brewer M, Zhu Q. Coregistered three-dimensional ultrasound and photoacoustic imaging system for ovarian tissue characterization. J Biomed Opt 2009;14(5):054014.

[15] Jaeger M, Harris-Birtill D, Gertsch A, O'Flynn E, Bamber J. Deformation-compensated averaging for clutter reduction in epiphotoacoustic imaging in vivo. J Biomed Opt 2012;17(6):066007.

[16] Fronheiser MP, Ermilov SA, Brecht HP, Conjusteau A, Su R, Mehta K, Oraevsky AA. Real-time optoacoustic monitoring and three-dimensional mapping of a human arm vasculature. J Biomed Opt 2010;15(2):021305.

[17] Zalev J, Clingman B, Herzog D, Miller T, Stavros AT, Oraevsky A, Kist K, Dornbluth NC, Otto P. Opto-acoustic breast imaging with co-registered ultrasound. Proc SPIE 2014;9038:90381J.

[18] Wurzinger G, Nuster R, Schmitner N, Gratt S, Meyer D, Paltauf G. Simultaneous three-dimensional photoacoustic and laser-ultrasound tomography. Biomed Opt Express 2013;4(8):1380–9.

[19] Nuster R, Schmitner N, Wurzinger G, Gratt S, Salvenmoser W, Meyer D, Paltauf G. Hybrid photoacoustic and ultrasound section imaging with optical ultrasound detection. J Biophotonics 2013;6(6–7):549–59.

[20] Ermilov SA, Khamapirad T, Conjusteau A, Leonard MH, Lacewell R, Mehta K, Miller T, Oraevsky AA. Laser optoacoustic imaging system for detection of breast cancer. J Biomed Opt 2009;14(2):024007.

[21] Bauer DR, Olafsson R, Montilla LG, Witte RS. 3-D photoacoustic and pulse echo imaging of prostate tumor progression in the mouse window chamber. J Biomed Opt 2011;16(2):026012.

[22] Yao J, Maslov KI, Zhang Y, Xia Y, Wang LV. Label-free oxygen-metabolic photoacoustic microscopy in vivo. J Biomed Opt 2011;16(7):076003.

[23] Zhang HF, Maslov K, Stoica G, Wang LV. Functional photoacoustic microscopy for high-resolution and noninvasive in vivo imaging. Nat Biotechnol 2006;24(7):848–51.

[24] Khokhlova TD, Pelivanov IM, Kozhushko VV, Zharinov AN, Solomatin VS, Karabutov AA. Optoacoustic imaging of absorbing objects in a turbid medium: ultimate sensitivity and application to breast cancer diagnostics. Appl Opt 2007;46(2):262–72.

[25] Manohar S, Kharine A, van Hespen JC, Steenbergen W, van Leeuwen TG. The twente photoacoustic mammoscope: system overview and performance. Phys Med Biol 2005;50(11):2543–57.

[26] Manohar S, Vaartjes SE, van Hespen JC, Klaase JM, van den Engh FM, Steenbergen W, van Leeuwen TG. Initial results of in vivo non-invasive cancer imaging in the human breast using near-infrared photoacoustics. Opt Express 2007;15(19):12277–85.

[27] Jaeger M, Frenz M, Schweizer D. Iterative reconstruction algorithm for reduction of echo background in optoacoustic images. Proc SPIE 2008;6856:68561C.

[28] Jaeger M, Siegenthaler L, Kitz M, Frenz M. Reduction of background in optoacoustic image sequences obtained under tissue deformation. J Biomed Opt 2009;14(5):054011.

[29] Jaeger M, Preisser S, Kitz M, Ferrara D, Senegas S, Schweizer D, Frenz M. Improved contrast deep optoacoustic imaging using displacement-compensated averaging: breast tumour phantom studies. Phys Med Biol 2011;56(18):5889–901.

[30] Jaeger M, Schüpbach S, Gertsch A, Kitz M, Frenz M. Fourier reconstruction in optoacoustic imaging using truncated regularized inverse k-space interpolation. Inverse Problems 2007;23:S51–63. http://iopscience.iop.org/0266-5611/23/6/S05/pdf/0266-5611_23_6_S05.pdf [Accessed on July 29, 2014].

[31] O'Donnell M, Skovoroda AR, Shapo BM, Emelianov SY. Internal displacement and imaging using ultrasonic speckle tracking. IEEE Trans Ultrason Ferroelectr Freq Control 1994;41(3):314–25.

[32] Frenz M, Jaeger M. Optimization of tissue irradiation in optoacoustic imaging using a linear transducer: theory and experiments. Proc SPIE 2008;6856:68561Y.

[33] Held G, Preisser S, Peeters S, Frenz M, Jaeger M. Effect of irradiation distance on image contrast in epi-optoacoustic imaging of human volunteers. Biomed Opt Express 2014. in press.